Nanoscale Analyses of X-ray Amorphous Material from Terrestrial Ultramafic Soils Record Signatures of Environmental Conditions Useful for Interpreting Past Martian Conditions

AD Feldman[1†], EM Hausrath[1], EB Rampe[2], TG Sharp[3], O Tschauner[1], A Lanzirotti[4], M Newville[4]

[1]Department of Geoscience, University of Nevada, Las Vegas, Las Vegas, Nevada 89154, U.S.A

[2]Astromaterials Research and Exploration Science Division, NASA Johnson Space Center, Houston, TX 77058, USA

[3]School of Earth and Space Exploration, Arizona State University, Tempe, AZ 85287, USA.

[4]Center for Advanced Radiation Sources, The University of Chicago, Chicago, IL, USA

Corresponding author: Anthony Feldman (anthony.feldman@dri.edu)

† Current address: Desert Research Institute, 755 East Flamingo Road, Las Vegas, NV 89119, USA

Key Points:

- The origin and environmental implications of Al-poor X-ray amorphous material in Gale crater and elsewhere on Mars remain unclear.
- We describe Mars-relevent X-ray amorphous material chemical heterogeneity in ultramafic soils in Mediterranean and subarctic climates.
- X-ray amorphous material forming under subarctic conditions is more chemically similar to Martian X-ray amorphous material.

Abstract

X-ray amorphous material that is variably Mg/Fe/Si-rich and Al-poor and that likely contains secondary alteration products is prevalent in Gale crater sediments and rocks (15-73 wt.%). However, the structure and origin of these materials and their implications for past environmental conditions remain unknown. In this study, we use transmission electron microscopy and synchrotron microprobe analyses to examine Mg/Fe/Si-rich and Al-poor ultramafic soils from the warm mediterranean climate Klamath Mountains of California and cold subarctic climate Tablelands of Newfoundland, Canada to help interpret environmental conditions during the formation of chemically similar X-ray amorphous material in Gale crater, Mars. Primary glass is absent from the Klamath Mountains and Tablelands materials; secondary X-ray amorphous material includes globular amorphous silica and chemically heterogeneous nanospherical amorphous material and nanocrystalline phases. Globular amorphous silica is only present in soils that undergo extensive periods of cyclic freezing. Fe-containing X-ray amorphous material from the subarctic Tablelands is significantly richer in Mg and Si than X-ray amorphous material from the warmer Klamath Mountains. Fe-rich nanocrystallites contain more Mg and Si in the subarctic Tablelands but are more highly Fe-enriched in the warmer Klamath Mountains. Potential secondary nanocrystalline phyllosilicates are only observed in the warmest examined soil in the Klamath Mountains. These characteristics – the presence or absence of amorphous silica, the chemical composition of X-ray amorphous material, the abundance and composition of Fe-rich nanocrystallites, and the presence or absence of secondary phyllosilicates - provide helpful identifiers to interpret past environmental conditions during the formation of X-ray amorphous material on Mars.

Plain Language Summary

The kinds of minerals and materials within martian rocks and loose sediments can provide clues to the conditions that were present during their alteration or production. X-ray amorphous material, material that lacks crystal structure as well as nanocrystallites less than roughly 100 nm in diameter, has been found in abundance within sediments and rocks at Gale crater on Mars. Beyond chemical data and abundance estimates, we do not know much about what this material is the implications of its presence for past environmental conditions. Therefore, we investigated the chemical and structural properties of chemically similar amorphous material in terrestrial soils developing under warm mediterannean and cold subarctic climatic conditions. Colder conditions correlate with greater magnesium and silica content and the presence of pure amorphous silica. Wamer conditions are associated with a lack of amorphous silica, lower magnesium and silica content within Fe-containing X-ray amorphous material, the formation of purely iron containing nanocrystallites, and the presence of nanocrystalline clay minerals. The chemical content of X-ray amorphous material forming under subarctic conditions is statistically more similar to that found at Gale crater. These results are consistent with the Gale crater X-ray amorphous material forming under generally cold and icy conditions.

1 Introduction

Analyses of X-ray diffraction data from the CheMin instrument on the Mars Science Laboratory rover have documented abundant (15-73 wt.%) X-ray amorphous material, likely encompassing amorphous material, short-range order phases, and nanocrystallites less than roughly 100 nm in diameter (Klug & Alexander, 1974; Smith & Horgan, 2021), in all ancient fluvial-lacustrine and aeolian rocks and modern aeolian sediments analyzed to date at Gale crater, Mars (Rampe et al., 2020; Thorpe et al., 2022). Mass balance calculations using CheMin mineral abundances and geochemical data from the Alpha Particle X-ray Spectrometer (APXS) instrument suggest that this X-ray amorphous material is variably Fe- (3.0 – 43.1 wt.% FeO_T) and Si-rich (3.6 – 75.9 wt.% SiO_2), Al-poor (≤10.46 wt.% Al_2O_3), sometimes Mg-rich (0.0 – 25.23 wt.% MgO) (Rampe et al., 2020; Smith et al., 2021; Thorpe et al., 2022), and contains secondary weathering products based on abundant volatile content (H_2O, CO_2, SO_2) measured by the Sample Analysis on Mars (SAM) instrument (Millan et al., 2022; Rampe et al., 2020). X-ray amorphous material can form through a variety of processes including volcanism (Nakagawa & Ohba, 2003), impact melting (Dressler & Reimold, 2001), anhydrous oxidation (Salvatore et al., 2019), aqueous alteration (Hiradate & Wada, 2005; Tutolo et al., 2019), and precipitation from aqueous solution (Ralston et al., 2021). While the formation mechanisms of the X-ray amorphous material in Gale crater remain poorly understood, inversely proportional FeO_T and SiO_2, SiO_2 that is directly proportional to total X-ray amorphous wt.% abundance, and potential primary glass contributions of ~0.1-57 wt.% are consistent with a substantial proportion of the Gale crater X-ray amorphous material being composed of aqueous alteration products (Smith et al. 2021).

Due to the typically Mg/Fe/Si-rich and Al-poor composition of serpentinized ultramafic bedrock, weathering of serpentinites produces secondary materials enriched in Mg/Fe/Si and depleted in Al (Baumeister et al., 2015; Caillaud et al., 2004; Rabenhorst et al., 1982). Previous work has utilized serpentinite-derived soils, sediments, and bedrock as analog settings for examining potential martian geochemical processes including the effects of climate and chemical mobility on the production of secondary clay minerals and Fe-oxides (Gaudin et al., 2011), the production of short-range order phyllosilicates during serpentinization processes (Tutolo et al., 2019), the potential for serpentinization processes to have abiotically contributed hydrogen (Greenberger et al., 2015) and methane (Szponar et al., 2013) to the early martian atmosphere, and the potential for serpentinization to produce clay and carbonate mineral assemblages similar to those found in Jezero crater (Grosch et al., 2021). Serpentinized minerals (serpentine and talc) have also been directly detected within Jezero crater where the Perseverance rover is currently caching samples for return to Earth (Farley et al., 2022; Liu et al., 2022), and the serpentine polymorph greenalite is potentially present in the sedimentary rocks at Glen Torridon in Gale crater (Thorpe et al., 2022). Serpentine soils therefore provide a useful Mg/Fe/Si-rich and Al-poor chemical environment for studying the influence of climatic variation on the development of Fe/Si-rich, sometimes Mg-rich, and Al-poor X-ray amorphous aqueous alteration products like those found in Gale crater and potentially elsewhere on Mars.

The prevalence of juvenile and X-ray amorphous secondary products on Mars has been proposed to indicate generally cold and icy, sometimes wet, conditions during formation (Rampe et al., 2022; Thorpe et al., 2021; Tosca & Knoll, 2009). Amorphous aluminosilicates such as allophane are typically thought to be transient phases that alter to more crystalline minerals over

time (Harsh et al., 2002; Wada, 1989). Previous work examining the formation and longevity of amorphous and short-range order aluminosilicates such as allophane in terrestrial field environments suggests that kinetically limiting conditions such as colder temperatures (Rampe et al., 2022; Rasmussen et al., 2010; Yesavage et al., 2015) or episodic high-intensity but short-duration aqueous alteration under generally highly arid conditions (Ziegler et al., 2003) can promote the formation and persistence of amorphous aluminosilicates. However, to our knowledge, no work to date has similarly examined the effects of temperature over time on the chemical heterogeneity of Mg/Fe/Si-rich but Al-poor X-ray amorphous material in terrestrial ultramafic soils that are chemically relevant to similarly Al-poor X-ray amorphous material on Mars.

Therefore, in this work soils from a suite of Mg/Fe/Si-rich and Al-poor ultramafic soils developing under the mediterranean climate of the Klamath Mountains of northern California and the subarctic climate of the Tablelands of Newfoundland, Canada were examined as analogs to the Fe/Si-rich, occasionally Mg-rich, and Al-poor X-ray amorphous material found in Gale crater, Mars. Bulk soil grain mounts were analyzed via synchrotron microprobe microfluorescence (μXRF), microdiffraction (μXRD), and X-ray absorption fine structure (XAFS) techniques. Results indicate that the presence of amorphous silica, greater Mg- and Si-incorporation within X-ray amorphous material coupled with a more limited formation of more purely Fe-containing nanocrystallites, and the absence of secondary phyllosilicates are consistent with colder conditions. By contrast the absence of amorphous silica, the formation of more purely Fe-containing X-ray amorphous material including Fe-(oxyhydr)oxide nanocrystallites, and the presence of secondary phyllosilicates are consistent with warmer conditions. These indicators may therefore be useful in interpreting aqueously altered materials on Mars and in samples returned from Mars.

2 Materials and Methods

2.1 Field Sites and Soil Material

Ultramafic soil samples were collected from two sites dubbed Eunice Bluff and String Bean Creek in the Klamath Mountains in August 2018 and from two sites dubbed Devil's Punchbowl and Trout River Gulch in the Tablelands of Gros Morne National Park on Newfoundland, Canada in October 2018 (Figure 1, Table S1). Temperature and precipitation averages from the Environment Canada continuous weather monitoring station in Cow Head, NL most proximal to the Tablelands indicate that the Tablelands have a mean annual temperature of <3.9 ºC and precipitation of ~120.4 cm/year water equivalents, with ~178 days with below freezing temperatures (Environment Canada, 2010). NOAA SNOTEL continuous climate monitoring stations at Weaverville, CA (elevation: ~610 m) and Sawyers Bar, CA (elevation: ~659 m) indicate that low- to mid-elevation regions of the Klamath Mountains as at String Bean Creek (~1,120 m) on average possess a mean annual temperature of ~12.8 ºC and water equivalent precipitation of ~101.2-117.6 cm/year with ~93 days per year experiencing below freezing temperatures though mean daily temperatures remain above freezing year-round (Arguez et al., 2010; Skinner et al., 2006). Climate data from a weather station on Red Rock Mountain at an elevation of 2042 m, coincident with Eunice Bluffs ~2100 m elevation, indicate that wintertime (defined as November-May) temperatures fluctuate between -19.4 ºC and 24.4 ºC (mean: 0.9 ºC) in high elevation regions of the Klamath Mountains while summertime (June-

October) temperatures remain relatively high (11.1 ºC to 31.6 ºC, mean: 12.7 ºC) (Garwood & Welsh, 2007). The number of days with below freezing temperatures at the Eunice Bluff site in the Klamath Mountains is therefore likely to be similar to or slightly greater than in the Tablelands on account of the higher altitude and a high degree of diurnal temperature variation (Arguez et al., 2010; Skinner et al., 2006); for example, precipitation in high elevation regions of the Klamath Mountains such as the Trinity Alps occurs predominantly as snowfall between November through May (Garwood & Welsh, 2007). The Klamath Mountains and Tablelands sites therefore have similar mean annual precipitation but varying temperature regimes, and the Tablelands sites and the higher elevation Klamath Mountain site experience substantially more days below freezing than the lower elevation Klamath Mountains site.

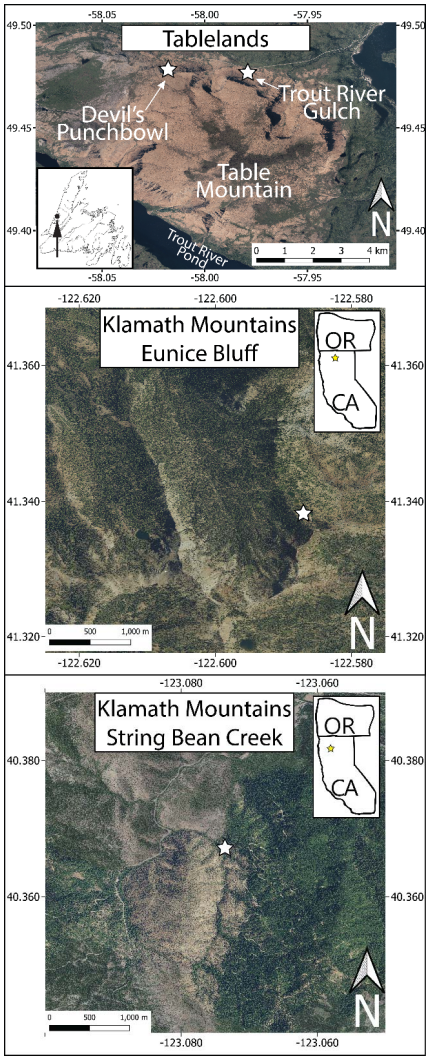

Figure 1. Soil sampling locations marked by white stars. Exact latitude, longitude, and elevation measurements are given in Table S1. Latitude and longitude (in decimal degrees), and elevation (in meters) for each site are as follows— Devil's Punchbowl: 49.480056, -58.016667, 292, Trout River Gulch: 49.479041, -57.980459, 155, Eunice Bluff: 41.339083, -133.587389, 2106, String Bean Creek: 40.367500, -123.073033, 1174.

Time since deglaciation is commonly used as a proxy for soil age and by extension the duration of soil weathering (Birkeland et al., 1991; Mahaney et al., 2009). The Klamath

Mountains Eunice Bluff soil was likely deglaciated ~12.1 ka based on paleolake records (Daniels et al., 2005) and cosmogenic dating of glacial deposits (Dickey, 2016) in the nearby Trinity Alps. The String Bean Creek soil in the Klamath Mountains is undated but developing in an area with no record of glaciation and is therefore likely substantially older than the Eunice Bluff soil. In the Tablelands, cosmogenic dating of boulders on a glacial moraine indicate that the Devil's Punchbowl location was deglaciated at ~17.6 ka while cosmogenic dating of debris bench material suggests the Trout River Gulch soil was deglaciated prior to ~20 ka (Osborn et al., 2007).

Soil samples from both the Klamath Mountains and the Tablelands locations were collected from soil pits excavated by hand using a pick and a shovel. Soil samples were selected from the visually most weathered part of each soil profile, B soil horizons when present and C soil horizons otherwise. Within the Klamath Mountains sites, samples were selected from a BC horizon of the Eunice Bluff soil (23-33 cm depth interval) which was dug to point of refusal (max depth: 53 cm), and from a Bt horizon of the String Bean Creek soil (40-50 cm depth interval) which was dug into the C horizon (max depth: 130 cm). Soils from the Tablelands (Devil's Punchbowl and Trout River Gulch) were not visually differentiated and were determined to possess only C-horizons. Bulk soil samples were collected from the midpoint of the Devil's Punchbowl soil (20-35 cm depth) that was dug to point of refusal (max depth: 50 cm), and from 35-50 cm depth in the Trout River Gulch soil pit which was dug until groundwater started to fill the soil pit (max depth: 70cm). Soil material utilized for preparation of polished thin section grain mounts for synchrotron analysis and for TEM analyses were prepared from the same sample from each soil pit (Table S1).

2.2 Synchrotron Analyses

For synchrotron microprobe analyses, bulk soil samples were air-dried, sieved to <2 mm, and prepared as grain mounts by Wagner Petrographics, Inc. To prepare the grain mounts, bulk soil material was embedded in Buehler EpoThin 2 epoxy onto fused silica glass slides, cut to a 30-micron thickness, and polished to a 0.25-micron level using technical grade odorless mineral spirits to limit potential chemical alteration during polishing.

X-ray microprobe analyses including μXRF, μXRD, and XANES were conducted on beamline GSECARS 13-ID-E at the Advanced Photon Source at the Argonne National Laboratory on the polished thin section grain mounts. Coupled μXRF/μXRD mapping was conducted using a 10-millisecond dwell time with a 1.5 μm x 1.5 μm beam focused by a Rh-coated Kirkpatrick-Baez focusing optics system with X-rays selected by a Si(111) cryo-cooled double-crystal monochromator. μXRF data were collected using a Canberra SXD-7 7-element Si drift detector (SDD) with Xspress3 electronics. μXRD patterns were collected in transmission geometry using a Dectris Eiger 1M detector. For the coupled μXRF/μXRD analyses, the wavelength of the incident X-ray microprobe beam was set to 0.6888 Å. Two coupled μXRF/μXRD map sites were collected from each of the Eunice Bluff and Devil's Punchbowl grain mounts and one from the String Bean Creek and Trout River Gulch grain mounts due to time constraints at the beamline, resulting in a total of 3 at each of the Klamath and Tablelands sites. μXRF/μXRD map locations were selected to encompass both potential secondary material and primary mineral grains (Figure 2). The μXRF/μXRD maps were processed using the Larch 0.9.64 GSE MapViewer software (Newville, 2013).

Based on elemental distributions in the μXRF maps, points for additional μXRD and XAFS analyses were selected to include both potential secondary material and primary minerals (Figure 2; Table 1). Single point μXRD measurements were collected at these selected spots for 10 seconds. The 2D μXRD area detector patterns from selected points were processed using the Dioptas 0.5.4 software (Prescher & Prakapenka, 2015) using CeO_2 as a calibration standard. Prior to phase ID and quantification, the contribution to each μXRD pattern from the glass slide and epoxy was removed by manually scaling the intensity of a 2D μXRD pattern collected from a reference area on the glass slide that contained epoxy but no soil material to fit the background of each μXRD measurement. Integration of the measured 2D μXRD patterns into 1D intensity vs 2θ patterns was done in Dioptas (Prescher & Prakapenka, 2015), allowing for confirmation that the 1D conversion of the glass and epoxy contribution matches the background portion of the 1D conversion of each 2D μXRD pattern. μXRD patterns that exhibited single-crystal like spots in 2D μXRD images, but did not possess powder-like rings, were excluded from analysis. When single crystal-like diffraction spots were visible in 2D images of μXRD measurements that also exhibited powder-like rings, the single crystal diffraction spots were masked prior to export of 1D XRD patterns for phase identification and Rietveld refinement. Phase identification was initially performed within Dioptas software (Prescher & Prakapenka, 2015) using Crystallography Open Database files (Graulis et al., 2009). Rietveld refinement following initial phase identification was performed in Profex 5.1 (Doebelin & Kleeberg, 2015) using files from the Crystallography Open Database (Graulis et al., 2009).

To examine Fe-oxidation states within primary minerals and secondary products, linear combination fits (LCFs) were performed on XAFS spectra using the Larch XAS Viewer software following energy calibration, background subtraction, and normalization (Newville, 2013). To determine the Fe-valence states of the analyzed phases from the measured XAFS spectra, LCFs were performed from 7100 to 7160 eV using measurements from the single-valence Fe^{2+} standards olivine (Fo_{80}), siderite, vivianite, and chromite, and goethite and ferrihydrite as Fe^{3+} standards. The olivine and chromite standards were taken from the XANES standards library included with the Hephaestus program in the Athena software suite; they were collected at the ALS 10.3.2 beamline and are from (Marcus et al., 2008). The siderite, vivianite, ferrihydrite, and goethite standards are from (Hansel et al., 2001) and were collected at the APS 13-ID-E beamline. All XAFS patterns used in fitting were adjusted for energy offsets prior to fitting. E0 was set for zero valent Fe, measured using an Fe-foil reference standard, to a value of 7110.518 eV. LCFs do not demonstrate that a particular measured spot is composed of the mineral standards utilized during fitting, but that the Fe valence state at the measured point is best modelled by a combination of pre-selected standards representing potential ferric and ferrous iron contributions. Linear combination fitting over the 7100 to 7160 eV range primarily involves fitting the white line portion of the XAS spectra (Kelly et al., 2015).

2.3 Transmission Electron Microscopy

For TEM analyses, the clay-size (<2 μm diameter) fraction was extracted from bulk soil material because incipient chemical alteration products including X-ray amorphous material concentrate in this size fraction (Yesavage et al., 2015). To separate the <2 μm size fraction from the bulk soil, 10 g of bulk soil were mixed with 25 mL of 18.2 MΩ DI water, sonicated for 30 minutes, vortexed, and allowed to settle for 1.5 hours after (Edwards & Bremner, 1967). The supernatant was pipetted off, ACS reagent grade NaCl was added to the supernatant to a

concentration of 1 M to promote flocculation, and the samples were allowed to settle for 30 minutes. Samples were then centrifuged for 3 minutes at 8,000 rpm (8,228 x g) and the clear supernatant was decanted from the clay-size fraction pellet. The clay-size fraction pellets were then washed by adding 18.2 MΩ DI water, agitating the samples, and centrifuging at 8,000 rpm 3 more times to remove residual salt, frozen at -20°C for at least 12 hours, freeze-dried, then stored at -20°C until analysis.

To prepare samples for TEM analysis, a small amount of the clay-size fraction was first added to ~15 mL of a 70% ethanol and 30% water solution. The solution was sonicated for 5 minutes to disperse clay-size particle aggregates. A carbon-coated copper TEM grid (Ted Pella Lacey Carbon Grids on 200 mesh Cu Grids, Part # 01894) was swirled in the ethanol and clay-size material suspension and allowed to air dry. Prepared samples were analyzed using a Titan 300/80 (FEI) aberration corrected TEM at 300 kV accelerating voltage with a field emission source and a Bruker XFlash 6T|30 electron dispersive spectroscopy (EDS) detector at the Eyring Materials Center at Arizona State University. This instrument uses a CETCOR Cs corrector for the objective lens to produce high resolution images with a spatial resolution of 0.7 Å. Imaging and diffraction data were collected with Gatan One-View 4x4k digital camera. The selected area aperture drive was not functioning properly during the available analysis time. While selected area electron diffraction (SAED) patterns were collected to determine crystallinity, the presence or absence of amorphous material was determined primarily from fast Fourier transform (FFT) diffractograms of high-resolution TEM images. The 300 keV high beam energy utilized can induce damage to sample material including causing sample materials to deform, shift, lose crystallinity (amorphization), or crystallize. All images used for determining the presence and characteristics of X-ray amorphous material (Figures 4-7, S59-S114), EDS measurements (Table 2, Appendix A), and d-spacing measurements (Table 3) are from TEM images and EDS measurements in which no evidence of beam damage was observed; data acquisition from any TEM imaging site was ended if beam damage was observed.

Due to the time-intensive nature of TEM work, 10 to 20 individual particles and particle clumps (referred to as TEM sites, see Table S2, Figures S59 – S114) from the TEM sample from each soil were examined to identify whether X-ray amorphous material was present and, if so, the structural and chemical characteristics were studied. To examine the full range of X-ray amorphous material, truly amorphous material and nanocrystallites were examined in a manner like (Smith & Horgan, 2021). Truly amorphous refers to material without lattice fringes in high-resolution TEM images and without discernable peaks or rings in SAED patterns or FFT diffractograms. Nanocrystalline materials were defined as containing crystal or ordered domains less than 100 nm in size that produce visible though typically diffuse peaks in SAED patterns or FFT diffractograms (Smith & Horgan, 2021). Nanocrystallites can be present within the X-ray amorphous component as XRD peaks become increasingly broad as crystallite size drops below ~100 nm (Klug & Alexander, 1974) and become indistinguishable from amorphous background scattering at crystallite sizes ≤10 nm (Holder & Schaak, 2019). TEM images, SAED patterns, and FFT diffractograms were examined using Gatan Micrograph 3 software.

EDS chemical measurements of the examined X-ray amorphous material were normalized to 100% without Cu or C due to potential contributions from the TEM grid material. EDS quantification utilized a standardless Cliff-Lorimer technique with theoretical K-factors. When possible, EDS measurements were acquired from areas that did not overlap with carbon

mesh material to limit the influence of carbon on chemical measurements. EDS measurement spot size varied by site from as little as several nanometers in diameter to several tens of nanometers across, and therefore the possibility exists that EDS measurements may have captured multiple materials within each EDS measurement zone. Care was taken to examine each TEM site during EDS acquisition for signs of beam damage induced changes; if beam damage was observed during EDS acquisition the spectrum was discarded. EDS Measurements were collected in TEM mode from materials determined to be amorphous and nanocrystalline from TEM imaging. After identification of amorphous or nanocrystalline material, a beam stop was put in place to limit sample electron exposure and potential beam damage from the 300 kV beam to preserve sample material for subsequent EDS measurements. Initially, one EDS measurement was typically collected from amorphous material or nanocrystallites at each TEM site provided beam damage was not observed. After initial confirmation that globular amorphous material was composed of amorphous silica (see results), EDS data were not collected from additional globular material (Table S2). At one TEM site from the Devil's Punchbowl soil in the Tablelands 3 EDS measurements were made on amorphous material from different points along a rim surrounding a phyllosilicate aggregate (Figure S104). This was the only site where more than one EDS measurement was acquired from amorphous material.

2.4 Statistical Analyses

A Shapiro-Wilk normality test was run on a) the oxidation state determined by LCF fits of the synchrotron data for examined primary and secondary materials from the Klamath Mountains and the Tablelands (i.e., all Klamath Mountain sites combined, all Tablelands sites combined), b) Fe, Si, and Mg concentrations from EDS data of X-ray amorphous material from the Klamath Mountains and the Tablelands (i.e., all Klamath Mountain sites combined, all Tablelands sites combined) and the Gale crater X-ray amorphous material, and c) Fe, Si, and Mg values for the individual amorphous and nanocrystalline components of the terrestrial X-ray amorphous material from the Klamath Mountains and the Tablelands (i.e., all Klamath Mountain sites combined, all Tablelands sites combined). If normality was not rejected at a 95% confidence level for all datasets being compared, then a two-sample t test was used when comparing two sample groups and a Tukey-honest difference test if comparing three sample groups. If normality was rejected at a 95% confidence level for at least one dataset being compared, then the dataset distributions were compared using non-parametric tests, a Kruskal-Wallis ANOVA test for comparing three sample groups or a Mann-Whitney test for comparing two sample groups. See the supplementary online material for a schematic flow chart and statistical analysis outputs (Figures S115-S140).

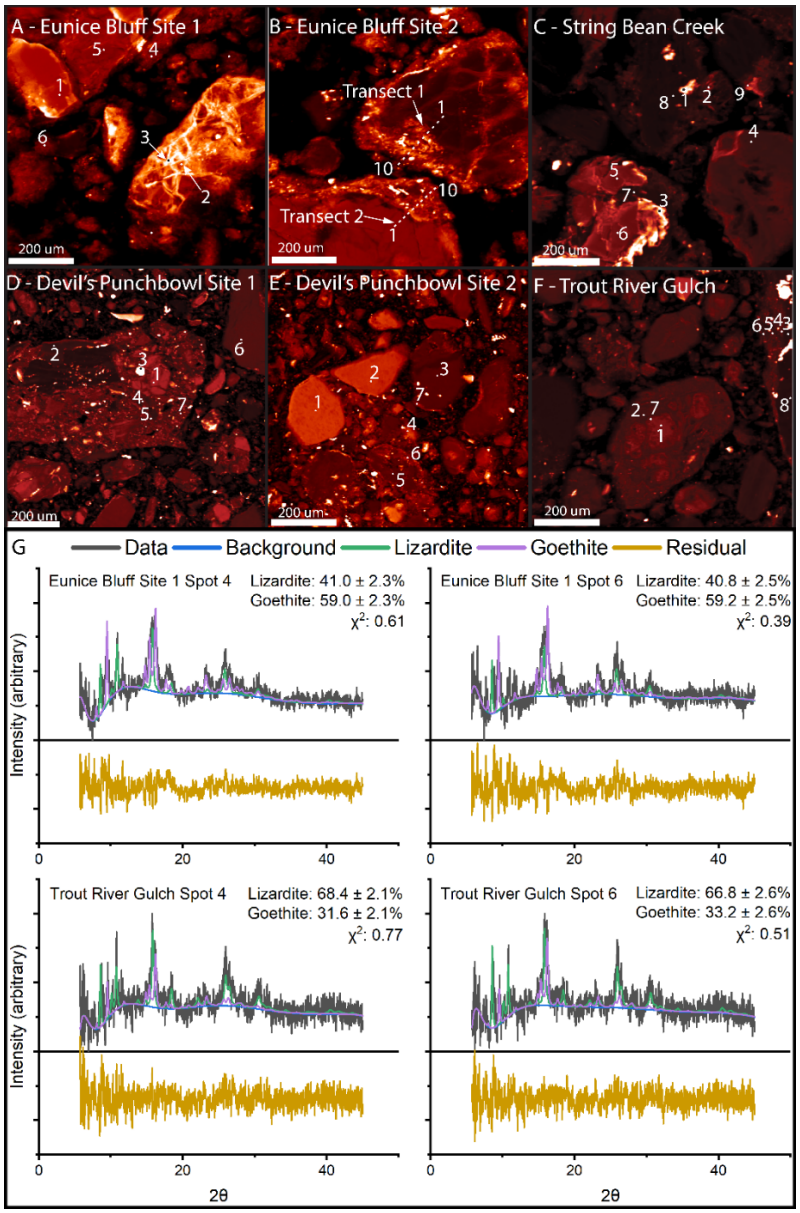

Figure 2. Synchtron microprobe results. A-F) µXRF heatmaps and XAFS/µXRD measurement spots from the Eunice Bluff soil (panels A and B) and String Bean Creek soil in the Klamath Mountains (panel C), and the Devil's Punchbowl soil (panels D and E) and the Trout River Gulch soil in the Tablelands (panel F). G) Rietveld fits of synchrotron µXRD patterns from weathering rinds from Eunice Bluff soil in the Klamath Mountains and the Trout River Gulch soil in the Tablelands. Phase abundances are given as wt.%, and the uncertainty is 2 standard deviations from the mean. Chi-squared values below 1 result from high degrees of noise in the fitted patterns due to the measurement times of 10 seconds.

3 Results

3.1 Synchrotron Microprobe

Synchrotron μXRF maps of thin sections of bulk soil material indicate that Fe is present throughout the bulk soil in both primary and secondary material (Figure 2A-2F). Rietveld refinements of μXRD patterns demonstrate the presence of lizardite and goethite in weathered soil material in both Tablelands and Klamath Mountain soils (Figure 2G) with goethite present in greater abundance in examined weathering rinds from the Klamath Mountains soils (59.0 ± 2.3 – 59.2 ± 2.5 wt.%) than the Tablelands soils (31.6 ± 2.1 – 33.2 ± 2.6 wt.%) (Figure 2G). Refinements could not be performed on 2D μXRD patterns acquired from primary minerals due to the lack of powder-like rings. Linear combination fits (LCF) of XAFS spectra (Appendix A; Figures S1-S58) from points within the coupled μXRF and μXRD maps (Figure 2) yield Fe oxidation states (Table 1) that contain statistically significantly higher Fe oxidation states than primary material (Figures S116 – S119).

Table 1. Fe-oxidation states derived from linear combination fitting of Fe XAFS patterns.

Spot #[a]	EB Site 1	EB Site 2 Transect 1	EB Site 2 Transect 2	SBC	DvP Site 1	DvP Site 2[b]	TRG
1	2.10	2.00	2.21	2.37	2.27	2.08	2.00
2	2.87	2.00	2.22	2.32	2.92	2.00	2.93
3	2.93	2.00	2.45	2.81	2.45	2.61	2.56
4	2.86*	2.64*	2.39	3.00	2.85*	2.72*	2.89*
5	2.13	2.81*	2.73*	2.10	2.60*	2.66*	2.93*
6	2.84*	2.87*	2.79*	2.13	2.67	2.95*	2.95*
7		2.89*	2.84*	2.91*	2.92*	2.75*	2.92
8		2.85*	2.82*	2.93			2.80
9		2.90*	2.86*	2.89*			
10		2.78*	2.87*				
Mean Fe Ox:	2.62 ± 0.39	2.57 ± 0.40	2.61 ± 0.27	2.60 ± 0.37	2.67 ± 0.25	2.54 ± 0.36	2.75 ± 0.33
Mean Prim. Ox:	2.51 ± 0.45	2.00 ± 0.00	2.32 ± 0.12	2.58 ± 0.38	2.58 ± 0.28	2.23 ± 0.33	2.64 ± 0.39
Mean Sec. Ox:	2.85 ± 0.14	2.82 ± 0.09	2.82 ± 0.05	2.90 ± 0.01	2.79 ± 0.17	2.77 ± 0.13	2.92 ± 0.03

[a] Spot # corresponds to transect and solo XAFS measurement points given in Figure 2.
Note: * Denotes weathering rind and/or potential secondary material, defined as diffuse Fe-containing regions surrounding or between relatively euhedral grains.

3.2 Transmission Electron Microscopy

X-ray amorphous material was observed in all samples analyzed by TEM. The X-ray amorphous component is composed of homogenous globular amorphous silica (Figure 3A) and a chemically heterogenous assortment of nanospherical amorphous (Figure 3B) and nanocrystalline material (Figure 3C). No examples of glassy textures were observed (i.e., angular X-ray amorphous grains with a homogeneous tone) that would indicate the presence of primary amorphous material.

The globular amorphous silica spherules are structurally and chemically homogenous, lack distinct lattice fringes in HRTEM images (Figure 3A), and possess no indications for the presence of crystallinity in the FFT and SAED diffractograms (Figure 3D). Some of the globular amorphous silica spherules deviate from perfectly spherical but always have rounded and well-defined edges (Figure 3A). EDS scans indicate that amorphous globulus are nearly pure SiO_2 with minor amounts (<3 atom %) of Mg, Fe, and Al (Table 2). Some amorphous silica globules

overlap crystalline material or other X-ray amorphous material, but amorphous silica globules are not observed intermixed with or growing out of crystalline or other amorphous materials. Globular material is present in 11 out of 27 examined sites from the two Tablelands soils in aggregates up to ~2 µm across and present in 10 out of 19 examined sites from the Eunice Bluff soil in the Klamath Mountains in aggregates up to ~400 nm across (e.g. Figure 4A - 4C). Globular amorphous silica was not observed in any of the 11 examined TEM sites from the String Bean Creek soil.

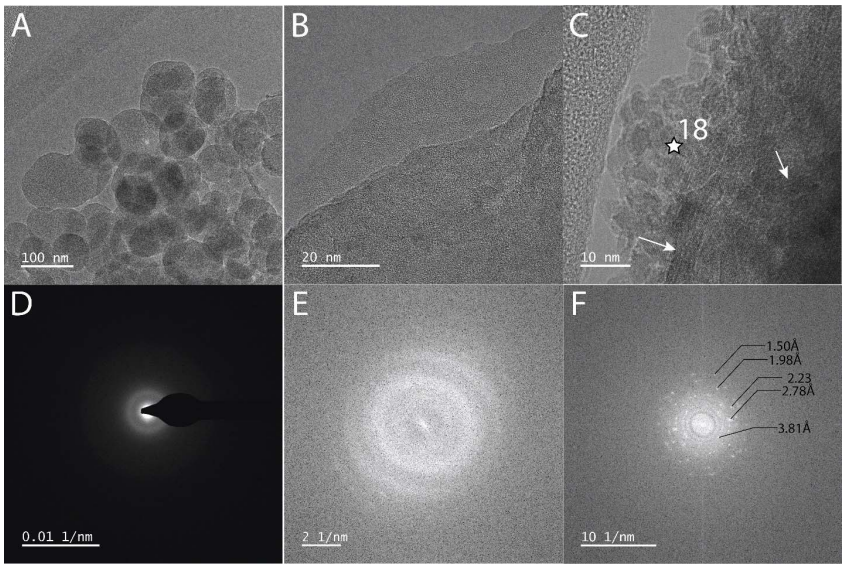

Figure 3. Examples of globular, clumpy nanospherical, and clumpy nanocrystalline X-ray amorphous material. The labelled star denotes an energy dispersive spectroscopy measurement point given in Table 3 and Figure 7. A) Globular amorphous material from the Devil's Punchbowl soil (DvP TEM site 15, Table S2) in the Tablelands. B) Nanospherical clumpy material from the Devil's Punchbowl site (DvP TEM Site 2: Table S2) in the Tablelands. C) Nanocrystalline clumpy material from the String Bean Creek site (SBC TEM Site 11: Table S2) in the Klamath Mountains, white arrows denote potential nanocrystalline phyllosilicates, labelled start is the location of an EDS measurement spot in Table 2. D) SAED diffractogram from the center of the mass of globules in Panel A. E) FFT diffractogram of panel B demonstrating material is X-ray amorphous. F) FFT diffractogram of panel C.

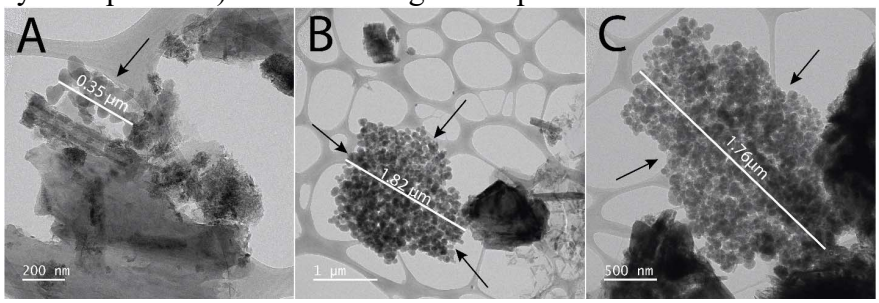

Figure 4. Size variation in globular amorphous silica accumulations. A) Globular amorphous silica from the Eunice Bluff soil (EB TEM site 17, see Table S2) in the Klamath Mountains. B-C) instances of agglomerations of hundreds of individual spherules of globular X-ray amorphous material in the Tablelands from the Devil's Punchbowl (B: DvP TEM site 10, see Table S2, C: DvP TEM site 12, see Table S2).

401 Table 2 – Major element abundances (atom %) for X-ray amorphous material measured by EDS

EDS Spot #[a]	Morphology	Location	Si	Fe	Mg	Al	O
			Klamath Mountains X-ray Amorphous Material				
1	Globular	Eunice Bluff	36.33 ± 1.13	0.00 ± 0.00	0.00 ± 0.00	0.00 ± 0.00	63.66 ± 1.96
2	Globular	Eunice Bluff	33.62 ± 0.52	0.00 ± 0.00	0.00 ± 0.00	0.00 ± 0.00	66.38 ± 1.77
3	Globular	Eunice Bluff	35.24 ± 0.39	0.18 ± 0.07	0.16 ± 0.05	0.00 ± 0.00	64.42 ± 1.63
4	Globular	Eunice Bluff	32.64 ± 0.29	0.59 ± 0.10	2.09 ± 0.12	0.31 ± 0.05	64.37 ± 1.59
5	Globular	Eunice Bluff	33.79 ± 0.35	0.00 ± 0.00	0.00 ± 0.00	0.00 ± 0.00	66.21 ± 1.68
6	Globular	Eunice Bluff	65.97 ± 1.75	0.37 ± 0.11	0.40 ± 0.08	0.42 ± 0.08	65.97 ± 1.75
		Averages:	34.08	0.19	0.44	0.12	65.17
		Standard Deviation:	1.44	0.25	0.82	0.19	1.15
7[b]	Nanospherical	Eunice Bluff	23.37 ± 0.62	13.25 ± 1.18	8.39 ± 0.43	0.00 ± 0.00	55.00 ± 1.45
8	Nanospherical	Eunice Bluff	22.65 ± 0.61	4.29 ± 0.56	3.48 ± 0.26	1.71 ± 0.19	67.50 ± 1.89
9	Nanospherical	Eunice Bluff	17.73 ± 0.77	6.95 ± 0.96	0.00 ± 0.00	3.77 ± 0.39	71.55 ± 2.27
10	Nanospherical	Eunice Bluff	9.22 ± 0.41	18.09 ± 1.53	1.72 ± 0.19	4.23 ± 0.32	66.24 ± 1.70
11	Nanospherical	String Bean Creek	14.15 ± 0.22	21.11 ± 1.41	1.06 ± 0.08	2.61 ± 0.14	58.24 ± 1.15
		Averages:	17.42	12.74	2.93	2.46	63.71
		Standard Deviation:	5.93	7.14	3.30	1.69	6.86
12	Nanocrystalline	Eunice Bluff	2.73 ± 0.18	24.60 ± 1.75	0.00 ± 0.00	3.37 ± 0.22	68.60 ± 1.50
13[b]	Nanocrystalline	Eunice Bluff	5.14 ± 0.29	21.08 ± 1.65	5.53 ± 0.32	4.70 ± 0.31	63.55 ± 1.56
14	Nanocrystalline	Eunice Bluff	3.48 ± 0.20	28.69 ± 1.91	0.00 ± 0.00	3.99 ± 0.24	63.52 ± 1.36
15	Nanocrystalline	Eunice Bluff	4.21 ± 0.13	29.31 ± 1.80	1.06 ± 0.08	2.00 ± 0.11	62.85 ± 1.16
16	Nanocrystalline	Eunice Bluff	4.36 ± 0.11	31.79 ± 1.85	0.04 ± 0.01	4.25 ± 0.17	58.46 ± 1.02
17	Nanocrystalline	Eunice Bluff	0.00 ± 0.00	39.86 ± 2.17	0.00 ± 0.00	2.81 ± 0.14	56.58 ± 0.98
18	Nanocrystalline	String Bean Creek	5.68 ± 0.24	38.99 ± 2.25	0.90 ± 0.11	1.82 ± 0.15	52.60 ± 1.07
		Averages:	3.66	30.62	1.08	3.28	60.88
		Standard Deviation:	1.89	6.95	2.02	1.12	5.33
			Tablelands X-ray Amorphous Material				
19	Globular	Devil's Punchbowl	33.76 ± 0.53	0.00 ± 0.00	0.34 ± 0.07	0.00 ± 0.00	65.90 ± 1.76
20	Globular	Devil's Punchbowl	34.52 ± 0.44	0.00 ± 0.00	0.00 ± 0.00	0.00 ± 0.00	65.48 ± 1.69
21	Globular	Trout River Gulch	35.15 ± 0.88	0.00 ± 0.00	0.82 ± 0.15	0.00 ± 0.00	64.03 ± 1.96
		Averages:	34.48	0.00	0.39	0.00	65.14
		Standard Deviation:	0.70	0.00	0.41	0.00	0.98
22[b]	Nanospherical	Devil's Punchbowl	39.01 ± 0.62	9.25 ± 0.78	18.15 ± 0.65	0.00 ± 0.00	32.62 ± 0.85
23	Nanospherical	Devil's Punchbowl	26.14 ± 0.41	9.77 ± 0.79	13.46 ± 0.49	0.00 ± 0.00	47.96 ± 1.10
24	Nanospherical	Devil's Punchbowl	33.25 ± 0.69	11.79 ± 0.67	17.47 ± 0.67	0.00 ± 0.00	35.57 ± 0.98
25	Nanospherical	Devil's Punchbowl	5.65 ± 0.18	26.95 ± 1.73	1.19 ± 0.10	1.21 ± 0.10	63.37 ± 1.24
26	Nanospherical	Trout River Gulch	14.48 ± 0.20	19.92 ± 1.12	3.67 ± 0.14	0.00 ± 0.00	48.77 ± 0.83
27	Nanospherical	Trout River Gulch	34.74 ± 0.72	7.56 ± 0.76	18.09 ± 0.73	0.00 ± 0.00	39.61 ± 1.12
		Averages:	25.88	14.54	12.09	0.20	0.88
		Standard Deviation:	12.67	7.94	7.55	0.49	0.77
28	Nanocrystalline	Devil's Punchbowl	19.83 ± 0.28	22.00 ± 1.41	5.73 ± 0.22	0.00 ± 0.00	51.23 ± 1.00
29	Nanocrystalline	Devil's Punchbowl	11.66 ± 0.22	25.66 ± 1.62	2.35 ± 0.13	0.00 ± 0.00	58.86 ± 1.13
30	Nanocrystalline	Trout River Gulch	10.99 ± 0.38	19.14 ± 1.49	8.43 ± 0.39	0.00 ± 0.00	61.44 ± 1.47
31	Nanocrystalline	Trout River Gulch	17.74 ± 0.51	16.50 ± 1.35	9.60 ± 0.45	0.00 ± 0.00	56.16 ± 1.41
		Averages:	15.06	20.83	6.53	0.00	56.92
		Standard Deviation:	4.40	3.93	3.22	0.00	4.36

402 [a] Spot # corresponds to labels in Figure 7.
403 [b] Spots 7, 13, and 22 are from Feldman et al. (Submitted)
404 Note: See Table S2 in the SOM for which TEM sites each EDS Spot # corresponds too.

405 A second X-ray amorphous component encompasses a heterogenous grouping of truly
406 amorphous, nanospherical material (Figure 3B) and nanocrystalline material (Figure 3C) that are
407 commonly but not universally found intermixed at the nanoscale (Figure 5), that lacks a regular
408 shape, possesses diffuse and rounded boundaries, and is chemically heterogenous.
409 Morphologically similar material lacking a well-defined euhedral shape and possessing diffuse
410 edges, sometimes with intermixed amorphous material and nanocrystallites, was termed "fluffy"
411 by Smith and Horgan (2021) and "clumpy" by Rampe et al. (2022), and we refer to this material
412 here as clumpy. Both nanospherical and nanocrystalline clumpy material is primarily observed
413 coating the edges of crystalline grains and crystalline aggregates (Figure 6A, 6B), although there
414 are two observed instances of isolated intermixed nanospherical and nanocrystalline aggregates
415 in the Eunice Bluff soil (e.g. Figure 6E-6H). In the Klamath Mountains, clumpy X-ray

amorphous material was observed in 10 out of 19 TEM sites from the Eunice Bluff soil and 1 out of 11 TEM sites from the String Bean Creek soil. In the Tablelands, clumpy X-ray amorphous material was observed in 4 out of 17 examined TEM sites from the Devil's Punchbowl soil and 4 out of 11 examined sites from the Trout River Gulch soil.

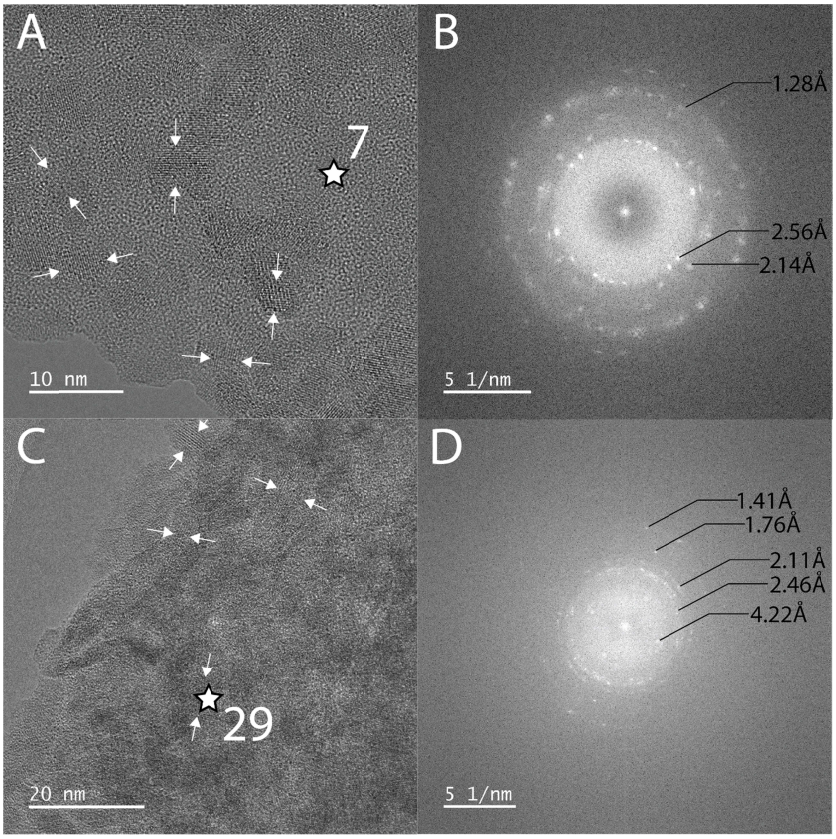

Figure 5. Intermixed nanospherical and nanocrystalline clumpy X-ray amorphous material. Panels show HRTEM imagery and associated fast Fourier transform (FFT) diffractograms of nanocrystalline domains within nanospherical material together comprising the clumpy morphology material. White arrows denote nanocrystalline domains. Labelled stars denote electron dispersive spectroscopy measurement spots given in Table 3, Figure 7, and Appendix A. A) Intermixed nanocrystalline and nanospherical clumpy material from the Eunice Bluff soil (EB Site 10: Table S2) in the Klamath Mountains B) FFT of panel A. C) Nanocrystalline packets intermixed in nanospherical clumpy material from the Devil's Punchbowl soil (DvP Site 15: Table S2) in the Tablelands. D) FFT of panel C.

The observed nanospherical material is composed of a mélange of tiny nodules (Figure 3B), morphologically like the "bubbly" texture of allophane (Iyoda et al., 2012; Ralston et al., 2021), consistent with formation as an aqueous alteration product. Nanospherical material is truly amorphous, lacking visible lattice fringes in HRTEM images (Figure 4B) or spots in FFT diffractograms (Figure 4E). Nanospherical clumpy material exhibits a high degree of chemical heterogeneity between aggregates, incorporating variable amounts of Si, Fe, Mg, and Al (Table 2), and minor amounts of other elements including Cr, Na, K, Ni, Ti, Mn, and Cl (Appendix B), but is on average more Si-rich than Fe-rich (Table 2).

Nanocrystalline clumpy material is primarily composed of packets of tiny, equant crystallites typically <20 nm across (Figure 3C, 4A, 4C). Although Si, Mg, and Al are present in variable amounts, nanocrystalline clumpy material in both the Klamath Mountains and Tablelands are uniformly Fe-rich (≥16.50 atom %) and, with one exception in the Tablelands, is more Fe-rich than Si-rich (Table 2).

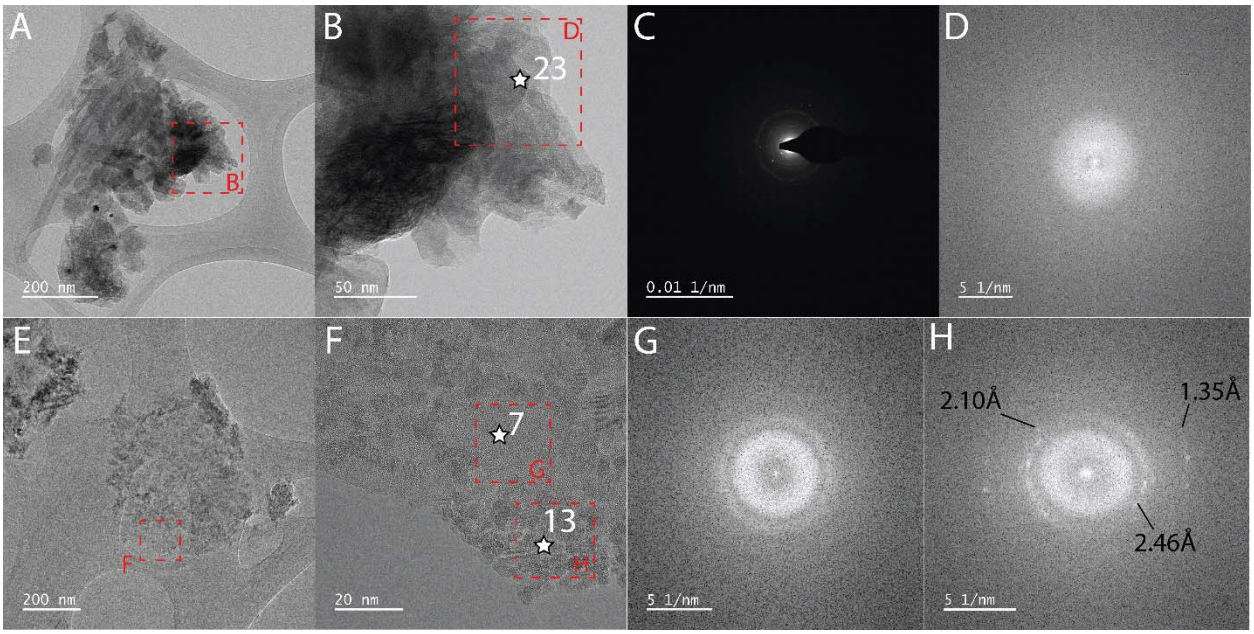

Figure 6. Examples of clumpy X-ray amorphous material on crystalline grain edges and as an independent particle. Clumpy nanospherical material forming at the edges of an aggregate of primary crystalline grains that includes phyllosilicate flakes and tubular serpentine, likely chrysotile, laths (A-D) and intermixed clumpy nanospherical and nanocrystalline material occurring as an isolated precipitate (E-H). Numbered white stars denote EDS measurement spots given in Table 3 and Figure 7. A) Aggregate mass of clay particles and amorphous material from the Devil's Punchbowl soil in the Tablelands (DvP TEM Site 17, Table S2). B) Higher magnification image of nanospherical amorphous material on the edge of the crystalline aggregate in panel A. C) Selected area electron diffractogram from the center of the crystalline mass in panel A. D) fast Fourier transform (FFT) diffractogram of nanospherical material shown in panel B. E) Isolated aggregate of intermixed nanospherical and nanocrystalline material from the Eunice Bluff soil in the Klamath Mountains (EB TEM Site 10, Table S2). F) Higher magnification image of intermixed nanospherical and nanocrystalline material from panel E. G) FFT diffractogram of nanocrystalline material from panel F. H) FFT diffractogram of nanocrystalline material from panel F.

Gale crater amorphous material is overall chemically similar to the X-ray amorphous material from the Tablelands and relatively dissimilar to Klamath Mountains X-ray amorphous material (Figure 7). At a 95% confidence interval, Fe, Si, and Mg concentrations from the Tablelands and Klamath Mountains clumpy X-ray amorphous material exhibit normal distributions for Fe content but not for Si and Mg content, and Gale crater X-ray amorphous material exhibits normality for Si and Mg but not for Fe (Figures S123 – S125). Therefore, a non-parametric Kruskal-Wallis ANOVA test was employed to examine differences in Fe, Si, and Mg content between the Tablelands, Klamath Mountains, and martian X-ray amorphous material. These tests indicate that Fe, Si, and Mg concentrations in the clumpy material from the Tablelands and Gale crater are statistically indistinguishable, that Si and Mg content is significantly elevated in X-ray amorphous material from the Tablelands compared to the Klamath Mountains while Fe content does not exhibit significant differences, and that Gale crater X-ray amorphous material exhibits significantly lower Fe and higher Si and Mg values than Klamath Mountain X-ray amorphous material (Figures S126 – S128).

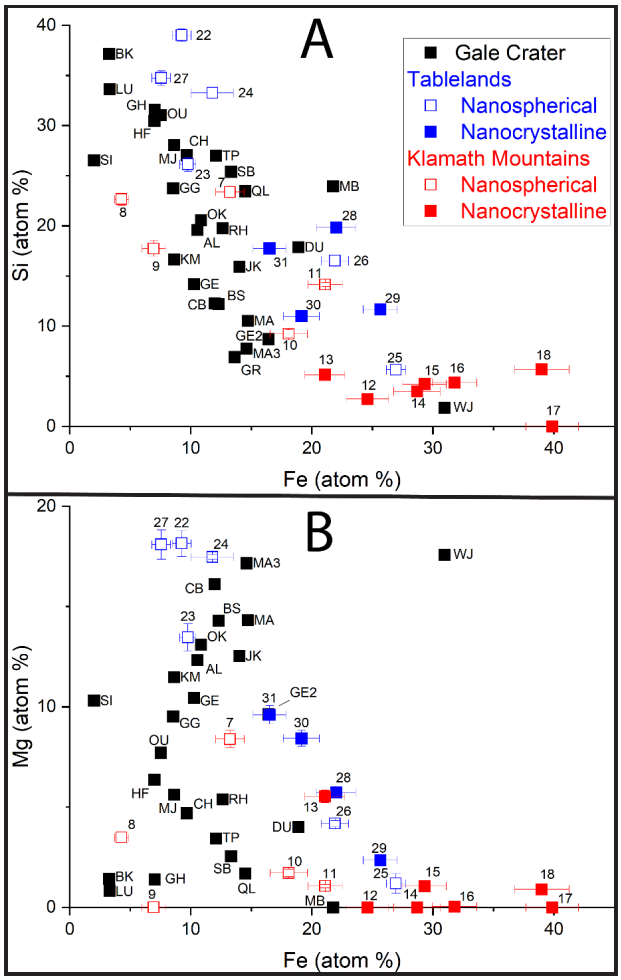

Figure 7. Plots of Si versus Fe (a) and Mg versus Fe (b) allow a comparison of the Si, Mg, and Fe concentrations of X-ray amorphous material from Gale crater (Rampe et al., 2020 and Thorpe et al., 2020), the Tablelands, and the Klamath Mountains. Gale crater and Tablelands amorphous material are not statistically differentiable, i.e. no statistically significant difference in Fe (Figure S126), Si (Figure S127), or Mg (Figure S128) content whereas the Gale crater and Klamath Mountains materials show a larger difference, i.e. statistically significant differences in Fe

(Figure S126), Si (Figure S127), and Mg (Figure S128). This result supports the inference that X-ray amorphous material in Gale crater is more likely to have formed in a colder environment. Gale crater X-ray amorphous material oxide wt.% chemistry and associated abbreviations can be found in (Rampe et al., 2020; Thorpe et al., 2022). EDS chemical data for terrestrial samples is given in Table 3.

Within the nanocrystallite component, while no nanocrystallites exhibit d-spacings representative of ideal ferric oxides and oxyhydroxides (Table 3), all nanocrystallites exhibit at least two lattice planes within 0.1 Å of d-spacings for the Fe^{3+}-oxyhydroxide goethite (Table 3); overlap between goethite and ferrihydrite peaks and potential growth of goethite from ferrihydrite precursors (Cudennec & Lecerf, 2006) suggest that ferrihydrite presence may also be present. Elongate curvilinear nanocrystallites with morphologies like the elongate curvilinear phyllosilicates observed by (Smith & Horgan, 2021) and (Rampe et al., 2022) in natural sediments and by (Ralston et al., 2021) forming within synthetic Fe-rich allophane were observed in clay-size fraction material from the String Bean Creek soil (Figure 3C). D-spacings from the associated FFT diffractogram (Figure 3F) were consistent with nontronite XRD peaks ~3.8 Å, 2.7 Å, and 2.2 Å (Baker & Strawn, 2014) and a ~1.5 Å peak consistent with the presence of a dioctahedral smectite (060) plane (Moore & Reynolds, 1997). These results suggest the presence of nanocrystalline smectites in the String Bean Creek soil clay-size fraction (Table 3). The presence of nanocrystalline smectites in the String Bean Creek soil is also consistent with the presence of smectites in the String Bean Creek soil clay-size fraction and bulk soil as determined by powder XRD (Feldman et al., Submitted for Review). Similar evidence for the presence of potential secondary nanocrystalline phyllosilicates within X-ray amorphous material was not observed in the Eunice Bluff soil or Tablelands soils.

Table 3. A summary of peak positions from the literature for ferrihydrite (F), goethite (G), and nontronite (N) compared to lattice fringe d-spacings for nanocrystalline domains where EDS measurements were taken (see Table 1 for EDS measurements)

Phase / TEM Site	EDS Spot #	d-spacings (Å)									Min ID
Ferrihydrite (6 line)[1]			4.5		3.2-3.3		2.51	2.25	1.98	1.73	1.48	F
Ferrihydrite (2 line)[1]						2.59					1.49	F
Ferrihydrite (Michel)[2]			4.57		3.41	2.62	2.47	2.24	1.96	1.64		F
Goethite (Anthony)[3]		4.98		4.18		2.64	2.45	2.25	2.19	1.72		G
Goethite (Nagai)[3]				4.20		2.70	2.46		2.20	1.73		G
Nontronite (BS)[4]		11.8			3.8	2.7		2.2				N
Eunice Bluff – Site 1	NA	5.22				2.59				1.72		F, G
Eunice Bluff – Site 2	NA			4.24		2.67				1.76		F, G
Eunice Bluff – Site 9	12						2.44		2.11	1.75	1.41	F, G
Eunice Bluff – Site 10	13						2.46		2.10		1.35	G
Eunice Bluff – Site 11	NA			4.37		2.86				1.71		F, G
Eunice Bluff – Site 16	14						2.47			1.75	1.53	F, G
Eunice Bluff – Site 17	15					2.72		2.19	1.92		1.50	F, G
Eunice Bluff – Site 18	16						2.45		2.01	1.67		F, G
Eunice Bluff – Site 19	17			4.19			2.42		2.16	1.69		F, G
String Bean Creek – Site 11	18				3.81	2.78		2.23	1.96		1.50	F, G, N
Devil's Punchbowl – Site 7	28				3.48		2.47		2.10	1.75		F, G
Devil's Punchbowl – Site 14	29			4.22			2.46		2.10	1.75	1.40	F, G
Trout River Gulch – Site 5	30		4.57				2.45	2.23			1.46	F, G
Trout River Gulch – Site 6	NA			4.01		2.67		2.24		1.79		F, G
Trout River Gulch – Site 7	31				3.57	2.67				1.79		G

[1]D-spacings for Ferrihydrite (6 line) and Ferrihydrite (2 line) are from Drits et al. (1993).

[2]D-spacings for Ferrihydrite (Michel) were extracted from published .cif files from recent work (Michel et al., 2007) suggesting the ferrihydrite structural model is like an Fe-substituted akdalaite structure.
[3]D-spacings for goethite are from the handbook for mineralogy (Anthony et al., 2001) and from Nagai et al. (2003)
[4]D-spacings for Nontronite (BS) are from Baker and Strawn (2014).
Note: TEM site #s correspond to site numbers given in Table S2 in the SOM. An EDS spot # of NA indicates that no EDS measurements were made.

4 Discussion

X-ray amorphous material represents a poorly understood aspect of martian mineral assemblages potentially useful as an indicator for past environmental conditions on Mars. The comparison of X-ray amorphous material from the subarctic climate Tablelands and the Mediterranean climate Klamath Mountain soils here indicates differences that provide important indicators for formation conditions for both returned samples and *in situ* analyses from Mars.

Globular amorphous silica is present in the high elevation (~2100 m) Eunice Bluff soil (Figure 4A) and the Tablelands soils (Figure 4B, 4C) that experience extended periods of freezing conditions (Garwood & Welsh, 2007) but not within the lower elevation String Bean Creek soil (~1120 m) that does not experience similar extended periods of sub-freezing conditions (Arguez et al., 2010; Skinner et al., 2006). Globular amorphous silica does not appear intermixed with or growing out of crystalline material, consistent with precipitation out of solution. The presence of amorphous silica only in soils where wintertime temperatures are consistently below freezing is consistent with lower temperatures decreasing amorphous SiO_2 solubility (e.g., Gunnarson and Arnórsson, 2000) coupled with freezing of soil-pore water increasing SiO_2 concentration in solution above amorphous SiO_2 saturation. Similar freeze thaw cycling has been demonstrated to promote amorphous silica precipitation in laboratory settings (Dietzel, 2005). Consistent with the proposed importance of freezing temperatures on globular amorphous silica formation, hydrated opaline silica coatings have been shown to be prevalent in glacially derived volcanic sediments forming under high-elevation cold climates in Cascadia from silica precipitating out of solution (Rutledge et al., 2018). Amorphous silica has also been documented within high-elevation cold climate pro-glacial soils and lake sediments from sites deglaciated after the Little Ice Age in the Three Sisters Volcanic complex in Oregon (Smith & Horgan, 2021) in cryogenic Antarctic soils (Simas et al., 2006), and in soils on the Arctic Archipelago of Svalbard (Hausrath et al., 2008). Amorphous silica therefore appears to be a robust indicator for the presence of extended periods of freeze-thaw conditions that could be useful in identifying the past presence of such conditions in samples returned from Mars.

The chemical composition of clumpy X-ray amorphous material likewise exhibits a robust relationship with temperature. Clumpy X-ray amorphous material in the subarctic Tablelands soils incorporates significantly greater amounts of Si and Mg than in the warmer Klamath Mountains soils (Figure 7, S127, S128) and is statistically undistinguishable from Gale crater X-ray amorphous material (Figures S126 – 128). Similar chemical trends are also apparent in the individual nanocrystalline and nanospherical components of the terrestrial soils, with nanocrystallite material in the subarctic Tablelands soils exhibiting significantly elevated Si and Mg and nanospherical material exhibiting significantly higher Mg-content than is found in

clumpy X-ray amorphous material in the warmer Klamath Mountains (Figures 7, S135 – S140). Greater incorporation of relatively immobile elements such as Fe into X-ray amorphous material and particularly into nanocrystallites in the warmer Klamath Mountain soils (e.g. Figure S138) while more mobile elements (Mg, Si) exhibit greater incorporation into X-ray amorphous material in the colder Tablelands soils is consistent with similarly Fe-containing, Mg-containing, but generally more Si-rich X-ray amorphous material in Gale crater (Rampe et al., 2020; Thorpe et al., 2022) forming under cold and wet conditions.

Fast Fourier transforms from all examined nanocrystallite-containing X-ray amorphous material exhibit at least two d-spacings within 0.1 Å of ideal d-spacings for the Fe^{3+}-oxyhydroxide goethite (Table 3); overlap between goethite and ferrihydrite peaks and potential growth of goethite from ferrihydrite precursors (Cudennec & Lecerf, 2006) suggest that ferrihydrite presence may also be present. The presence of goethite nanocrystallites indicated by d-spacings in TEM analyses is consistent with the presence of goethite in μXRD of Klamath Mountain soil weathering rinds (59.0 ± 2.3 – 59.2 ± 2.5 wt.%) and in the Tablelands soils (31.6 – 33.2 ± 2.6 wt.%) (Figure 2F). The more Fe-rich nature of the nanocrystallites in the Klamath mountains (Figures 7A, S135) than the Tablelands (Figures 7A, S136) could therefore be due to the greater presence of goethite observed in the synchrotron analyses.

Elongate curvilinear nanocrystallites, morphologically consistent with nanocrystalline phyllosilicates (Rampe et al., 2022; Smith & Horgan, 2021), with lattice fringe d-spacings consistent with observed XRD peaks for the Fe-rich dioctahedral smectite nontronite at ~3.8 Å, ~2.7 Å, and ~2.2 Å (Baker & Strawn, 2014), and ~1.5 Å (Moore & Reynolds, 1997) are only observed in the String Bean Creek soil (Figure 3C, Table 3). The String Bean Creek soil has been developing under a warmer climate (mean annual temperature: ~12.8 ºC) than all other soils examined in this study (Eunice Bluff: mean annual temperature <12.8 ºC, Tablelands soils: mean annual temperature <3.9 ºC) that likely lacks substantial periods of below freezing conditions (Skinner et al., 2006), and due to a lack of documented glaciation in the southern Klamath Mountains has likely been undergoing pedogenesis for a longer time period than the other examined soils. The presence of nanocrystalline smectites only within the oldest and warmest soil is consistent with previous work demonstrating that longer durations of aqueous alteration under warmer temperatures promote smectite formation (e.g., Bishop et al. 2018). The presence of secondary nanocrystalline phyllosilicates within the X-ray amorphous component is potentially consistent with incipient smectite development from amorphous precursors, like previous work in Klamath Mountain serpentine soils that proposed formation of smectites from amorphous gel precursors (Istok & Harward, 1982).

Secondary X-ray amorphous material in Fe-rich and Al-poor environments chemically relevant to past martian aqueous alteration suggest temperature indicators that will be valuable for analyzing samples returned from Mars. Detection of globular amorphous silica and mixed composition nanospherical and nanocrystalline material with high concentrations of mobile elements (e.g., Mg, Si) would be consistent with colder alteration conditions where freezing may occur seasonally, whereas an absence of amorphous silica, more purely Fe-rich nanocrystallites with lower incorporation of more mobile (Mg, Si) elements, and the presence of secondary phyllosilicates would be indicators of warmer conditions where freezing temperatures are uncommon.

Although the scales of observation are different, the chemical trends observed here can also assist in interpreting remote and *in-situ* observations of X-ray amorphous material on Mars for clues to temperature conditions during formation. In these examined terrestrial soils, the presence of amorphous silica correlates with seasonal sub-freezing conditions. That result is consistent with amorphous silica in Gale crater sediments (Rampe et al., 2020), at Gusev crater (Ruff & Hamilton, 2017), Jezero crater (Tarnas et al., 2019), and elsewhere across the martian surface (Milliken et al., 2008) resulting from precipitation from silica-rich fluids under predominantly cold and icy conditions, as has been proposed for hydrated amorphous silica fracture halos within Gale crater (Gabriel et al., 2023). Greater Si abundance within Fe-containing X-ray amorphous material from colder regions is consistent with the typically greater concentrations of Si than Fe within Gale crater X-ray amorphous material (Rampe et al., 2020; Smith et al., 2021; Thorpe et al., 2022) resulting from formation under cold and alternately wet and icy conditions. The coupled presence of Fe-rich nanocrystallites within a more Si-rich nanospherical amorphous matrix and pure amorphous silica in the subarctic Tablelands soils is compositionally and chemically like the mixed nanophase Fe-oxide and amorphous silica assemblage present in Gusev crater previously suggested to result from aqueous alteration under a relatively cold climate (Ruff & Hamilton, 2017). Nanocrystalline smectites in these Al-poor soils are only found in the warmest and oldest soil environment that lacks extended periods of sub-freezing conditions, consistent with the abundant smectites in Gale crater (T F Bristow et al., 2021; Thomas F. Bristow et al., 2018; Rampe et al., 2020; Thorpe et al., 2022) and elsewhere on the martian surface (Ehlmann & Edwards, 2014) indicating at least intermittent warm periods (Bishop et al., 2018).

5 Conclusions

The nature of Mars' early climate and aqueous conditions are imprinted in the secondary mineral assemblage, including in X-ray amorphous material, present in abundances up to 73 wt.% in Gale crater ancient fluviolacustrine and aeolian sedimentary rocks (Rampe et al., 2020; Thorpe et al., 2022). Transmission electron microscopy and synchrotron microprobe techniques results from the X-ray amorphous material from the cold subarctic climate of the Tablelands of Newfoundland Canada and the warmer Mediterranean climate of the Klamath Mountains of California demonstrate clear temperature-related trends in the composition of these materials. The formation of amorphous silica and greater retention of the more mobile Si and Mg cations (Gaudin et al., 2011) within Fe-containing X-ray amorphous material, particularly in the formation of mixed-composition nanocrystallites, is observed under colder conditions. Warmer conditions correlate with the formation of Fe-rich but relatively Mg- and Si-poor X-ray amorphous material and greater formation of more Fe-rich Fe^{3+}-oxyhydroxide nanocrystallites and promote the formation of nanocrystalline phyllosilicates.

These results are consistent with formation of the abundant Fe- and Si-rich but generally more Si- than Fe-rich, sometimes Mg-rich, and Al-poor X-ray amorphous material in Gale crater (Rampe et al., 2020; Thorpe et al., 2022) and X-ray amorphous material elsewhere on Mars (Ruff & Hamilton, 2017; Weitz et al., 2014) forming through aqueous alteration under generally cold and alternately icy and wet conditions. Abundant amorphous silica formation and incorporation of SiO_2 into X-ray amorphous material in returned martian samples, especially into nanocrystallite containing material, would further support formation under cold aqueous alteration conditions. This work demonstrates the influence of temperature conditions on the

structure and chemistry of X-ray amorphous material and that the chemical composition of such material could provide a useful proxy for estimating environmental conditions during formation in terrestrial and martian settings. Microscale analyses such as those presented here will be essential for evaluating returned martian samples and interpreting the implications of mineralogical and chemical heterogeneity in terms of past martian environmental conditions.

Acknowledgments

Funding for this project was provided by the National Aeronautics and Space Administration under grant No. 80NSSC20M0043 and grant No. NNX15AI02H. Funding was also provided by the UNLV Jack and Fay Ross family fellowship, the TTDGRA programs, the UNLV Geoscience Department, and the University of Nevada Las Vegas Graduate and Professional Student Association. Portions of this work were performed at GeoSoilEnviroCARS (The University of Chicago, Sector 13), Advanced Photon Source (APS), Argonne National Laboratory. GeoSoilEnviroCARS is supported by the National Science Foundation – Earth Sciences (EAR – 1634415) and NASA's Planetary Major Enabling Facilities (PSEF) program (grant number 80NSSC23K0196). This research used resources of the Advanced Photon Source, a U.S. Department of Energy (DOE) Office of Science User Facility operated for the DOE Office of Science by Argonne National Laboratory under Contract No. DE-AC02-06CH11357.

Conflict of Interest Statement

The authors declare no conflicts of interest relevant to this study.

Open Research

Climate data from the National Oceanic and Atmospheric Administration (NOAA) Snotel 1991-2020 and 1981 to 2010 climate normals (Arguez et al., 2010) and from the 1981-2010 Environment Canada climate normals were utilized in the creation of this manuscript (Environment Canada,

663 2010). Maps were created using QGIS software (QGIS Development Team, 2023). Statistical
664 analyses were conducted in OriginPro software (OriginLab Corporation, 2023).

665 ## References

666 Anthony, J. W., Bideaux, R. A., Bladh, K. W., & Nichols, M. C. (2001). *Handbook of mineralogy, mineralogical*
667 *society of America*. *Chantilly, VA20151-1110. USA* (Vol. Full Set).
668 Arguez, A., Durre, I., Applequist, S., Squires, M., Vose, R., Yin, X., & Bilotta, R. (2010). NOAA's U.S. Climate
669 Normals (1981-2020). *NOAA National Centers for Environmental Information*. NOAA National Centers for
670 Environmental Information. https://doi.org/10.7289/V5PN93JP
671 Baker, L. L., & Strawn, D. G. (2014). Temperature effects on the crystallinity of synthetic nontronite and
672 implications for nontronite formation in Columbia river basalts. *Clays and Clay Minerals*, *62*(2), 89–101.
673 https://doi.org/10.1346/CCMN.2014.0620202
674 Baumeister, J. L., Hausrath, E. M., Olsen, A. A., Tschauner, O., Adcock, C. T., & Metcalf, R. V. (2015).
675 Biogeochemical weathering of serpentinites: An examination of incipient dissolution affecting serpentine soil
676 formation. *Applied Geochemistry*, *54*, 74–84. https://doi.org/10.1016/j.apgeochem.2015.01.002
677 Birkeland, P. W., Berry, M. E., & Swanson, D. K. (1991). Use of soil catena field data for estimating relative ages of
678 moraines. *Geology*, *19*(3), 281–283. https://doi.org/10.1130/0091-7613(1991)019<0281:UOSCFD>2.3.CO
679 Bishop, J. L., Fairén, A. G., Michalski, J. R., Gago-Duport, L., Baker, L. L., Velbel, M. A., et al. (2018). Surface
680 clay formation during short-term warmer and wetter conditions on a largely cold ancient Mars. *Nature*
681 *Astronomy*, *2*(3), 206–213. https://doi.org/10.1038/s41550-017-0377-9
682 Bristow, T F, Grotzinger, J. P., Rampe, E. B., Cuadros, J., Chipera, S. J., Downs, G. W., et al. (2021). Brine-driven
683 destruction of clay minerals in Gale crater, Mars. *Science*, *373*(6551), 198–204.
684 https://doi.org/10.1126/science.abg5449
685 Bristow, Thomas F., Rampe, E. B., Achilles, C. N., Blake, D. F., Chipera, S. J., Craig, P., et al. (2018). Clay mineral
686 diversity and abundance in sedimentary rocks of Gale crater, Mars. *Science Advances*, *4*(6), 1–9.
687 https://doi.org/10.1126/sciadv.aar3330
688 Caillaud, J., Proust, D., Righi, D., & Martin, F. (2004). Fe-rich clays in a weathering profile developed from
689 serpentinite. *Clays and Clay Minerals*, *52*(6), 779–791. https://doi.org/10.1346/CCMN.2004.05206013
690 Cudennec, Y., & Lecerf, A. (2006). The transformation of ferrihydrite into goethite or hematite, revisited. *Journal of*
691 *Solid State Chemistry*. https://doi.org/10.1016/j.jssc.2005.11.030
692 Daniels, M. L., Anderson, S., & Whitlock, C. (2005). Vegetation and fire history since the Late Pleistocene from the
693 Trinity Mountains, northwestern California, USA. *The Holocene*, *15*(7), 1062–1071.
694 https://doi.org/10.1191/0959683605hl878ra
695 Dickey, N. W. (2016). *Chronology and Paleoclimate of Late Pleistocene Glaciation in The Klamath Mountains, CA*.
696 Colorado State University, Northridge.
697 Dietzel, M. (2005). Impact of cyclic freezing on precipitation of silica in Me–SiO2–H2O systems and geochemical
698 implications for cryosoils and -sediments. *Chemical Geology*, *216*(1–2), 79–88.
699 https://doi.org/10.1016/J.CHEMGEO.2004.11.003
700 Doebelin, N., & Kleeberg, R. (2015). Profex: A graphical user interface for the Rietveld refinement program
701 BGMN. *Journal of Applied Crystallography*, *48*, 1573–1580. https://doi.org/10.1107/S1600576715014685
702 Dressler, B. O., & Reimold, W. U. (2001). Terrestrial impact melt rocks and glasses. *Earth-Science Reviews*, *56*(1–
703 4). https://doi.org/10.1016/S0012-8252(01)00064-2
704 Drits, V. A., Sakharov, B. A., Salyn, A. L., & Manceau, A. (1993). Structural Model for Ferrihydrite. *Clay Minerals*,
705 *28*(2). https://doi.org/10.1180/claymin.1993.028.2.02
706 Edwards, A. P., & Bremner, J. M. (1967). Dispersion of Soil Particles By Sonic Vibration. *Journal of Soil Science*,
707 *18*(1), 47–63. https://doi.org/10.1111/j.1365-2389.1967.tb01487.x
708 Ehlmann, B. L., & Edwards, C. S. (2014). Mineralogy of the Martian Surface. *Annual Review of Earth and*
709 *Planetary Sciences*, *42*(1), 291–315. https://doi.org/10.1146/annurev-earth-060313-055024
710 Environment Canada. (2010). Canadian Climate Normals 1981-2010 Station Data. Cow Head. Climate ID:
711 8401335. Environment Canada.
712 Farley, K. A., Stack, K. M., Shuster, D. L., Horgan, B. H. N., Hurowitz, J. A., Tarnas, J. D., et al. (2022). Aqueously
713 altered igneous rocks sampled on the floor of Jezero crater, Mars. *Science*.
714 https://doi.org/10.1126/science.abo2196

Feldman, A., Hausrath, E., Rampe, E., Tu, V., Peretyazhko, T., DeFelice, C., & Sharp, T. (2023). Fe-rich X-Ray Amorphous Material Records Past Climate and Persistence of Water on Mars. *Submitted For Review*.

Gabriel, T. S. J., Hardgrove, C., Achilles, C. N., Rampe, E. B., Rapin, W. N., Nowicki, S., et al. (2023). On an Extensive Late Hydrologic Event in Gale Crater as Indicated By Water-Rich Fracture Halos. *Journal of Geophysical Research: Planets*, *127*(12). https://doi.org/https://doi.org/10.1029/2020JE006600

Garwood, J. M., & Welsh, H. H. (2007). *Ecology of the Cascades Frog (Rana cascadae) and Interactions with Garter Snakes and Nonnative Trout in the Trinity Alps Wilderness, California*.

Gaudin, A., Dehouck, E., & Mangold, N. (2011). Evidence for weathering on early Mars from a comparison with terrestrial weathering profiles. *Icarus*, *216*(1), 257–268. https://doi.org/10.1016/j.icarus.2011.09.004

Graulis, S., Chateigner, D., Downs, R. T., Yokochi, A. F. T., Quirós, M., Lutterotti, L., et al. (2009). Crystallography Open Database - An open-access collection of crystal structures. *Journal of Applied Crystallography*, *42*(4). https://doi.org/10.1107/S0021889809016690

Greenberger, R. N., Mustard, J. F., Cloutis, E. A., Pratt, L. M., Sauer, P. E., Mann, P., et al. (2015). Serpentinization, iron oxidation, and aqueous conditions in an ophiolite: Implications for hydrogen production and habitability on Mars. *Earth and Planetary Science Letters*, *416*, 21–34. https://doi.org/10.1016/j.epsl.2015.02.002

Grosch, E. G., Bishop, J. L., Mielke, C., Maturilli, A., & Helbert, J. (2021). Early Archean alteration minerals in mafic-ultramafic rocks of the Barberton greenstone belt as petrological analogs for clay mineralogy on Mars. *American Mineralogist*, *106*(5). https://doi.org/10.2138/am-2021-7656

Hansel, C. M., Fendorf, S., Sutton, S., & Newville, M. (2001). Characterization of Fe plaque and associated metals on the roots of mine-waste impacted aquatic plants. *Environmental Science and Technology*, *35*(19). https://doi.org/10.1021/es0105459

Harsh, J., Chorover, J., & Nizeyimana, E. (2002). Allophane and Imogolite. In *Soil Mineralogy with environmental applications 7* (pp. 291–322). https://doi.org/10.2136/sssabookser7.c9

Hausrath, E. M., Treiman, A. H., Vicenzi, E., Bish, D. L., Blake, D., Sarrazin, P., et al. (2008). Short- and Long-Term Olivine Weathering in Svalbard: Implications for Mars. *Astrobiology*, *9*(6), 1079–1092. https://doi.org/10.1089/ast.2007.0195

Hiradate, S., & Wada, S. I. (2005). Weathering process of volcanic glass to allophane determined by 27Al and 29Si solid-state NMR. *Clays and Clay Minerals*, *53*(4), 401–408. https://doi.org/10.1346/CCMN.2005.0530408

Holder, C. F., & Schaak, R. E. (2019, July 23). Tutorial on Powder X-ray Diffraction for Characterizing Nanoscale Materials. *ACS Nano*. American Chemical Society. https://doi.org/10.1021/acsnano.9b05157

Istok, J. D. D., & Harward, M. E. E. (1982). Influence of Soil Moisture on Smectite Formation in Soils Derived from Serpentinite. *Soil Science Society of America Journal*, *46*(5), 1106–1108.

Iyoda, F., Hayashi, S., Arakawa, S., Baiju, J., Okamoto, M., Hayashi, H., & Guodong, Y. (2012). Synthesis and adsorption characteristics of hollow spherical allophane nano-particles. *Applied Clay Science*, *56*, 77–83. https://doi.org/10.1063/1.4873773

Kelly, S. D., Hesterberg, D., & Ravel, B. (2015). Analysis of soils and minerals using x-ray absorption spectroscopy. In *Methods of Soil Analysis, Part 5: Mineralogical Methods* (Vol. 5). https://doi.org/10.2136/sssabookser5.5.c14

Klug, H. P., & Alexander, L. E. (1974). *X-ray Diffraction Procedures: for Polycrystalline and Amorphous Materials* (2nd ed.). Wiley.

Liu, Y., Tice, M. M., Schmidt, M. E., Treiman, A. H., Kizovski, T. V., Hurowitz, J. A., et al. (2022). An olivine cumulate outcrop on the floor of Jezero crater, Mars. *Science*. https://doi.org/10.1126/science.abo2756

Mahaney, W. C., Kalm, V., Kapran, B., Milner, M. W., & Hancock, R. G. V. (2009). A soil chronosequence in Late Glacial and Neoglacial moraines, Humboldt Glacier, northwestern Venezuelan Andes. *Geomorphology*, *109*, 236–245. https://doi.org/10.1016/j.geomorph.2009.03.005

Marcus, M. A., Westphal, A. J., & Fakra, S. C. (2008). Classification of Fe-bearing species from K-edge XANES data using two-parameter correlation plots. *Journal of Synchrotron Radiation*, *15*(5). https://doi.org/10.1107/S0909049508018293

Michel, F. M., Ehm, L., Antao, S. M., Lee, P. L., Chupas, P. J., Liu, G., et al. (2007). The structure of ferrihydrite, a nanocrystalline material. *Science*, *316*(5832). https://doi.org/10.1126/science.1142525

Millan, M., Williams, A. J., McAdam, A. C., Eigenbrode, J. L., Steele, A., Freissinet, C., et al. (2022). Sedimentary Organics in Glen Torridon, Gale Crater, Mars: Results From the SAM Instrument Suite and Supporting Laboratory Analyses. *Journal of Geophysical Research: Planets*, *127*(11). https://doi.org/10.1029/2021JE007107

Milliken, R. E., Swayze, G. A., Arvidson, R. E., Bishop, J. L., Clark, R. N., Ehlmann, B. L., et al. (2008). Opaline silica in young deposits on Mars. *Geology*, *36*(11). https://doi.org/10.1130/G24967A.1

Moore, D. M., & Reynolds, R. C. (1997). *X-ray Diffraction and the Identification and Analysis of Clay Minerals* (Second Edi). New York: Oxford University Press.

Nagai, T., Kagi, H., & Yamanaka, T. (2003). Variation of hydrogen bonded O...O distances in goethite at high pressure. *American Mineralogist*, *88*(10), 1423–1427. https://doi.org/10.2138/am-2003-1005

Nakagawa, M., & Ohba, T. (2003). Minerals in Volcanic Ash 1: Primary Minerals and Volcanic Glass. *Global Environmental Research*, *6*(October).

Newville, M. (2013). Larch: An analysis package for XAFS and related spectroscopies. In *Journal of Physics: Conference Series* (Vol. 430). https://doi.org/10.1088/1742-6596/430/1/012007

OriginLab Corporation. (2023). Origin(Pro). Northampton, MA, USA.

Osborn, G., Spooner, I., Gosse, J., & Clark, D. (2007). Alpine glacial geology of the Tablelands, Gros Morne National Park, Newfoundland. *Canadian Journal of Earth Sciences*, *44*(6), 819–834. https://doi.org/10.1139/e07-016

Prescher, C., & Prakapenka, V. B. (2015). DIOPTAS: A program for reduction of two-dimensional X-ray diffraction data and data exploration. *High Pressure Research*, *35*(3). https://doi.org/10.1080/08957959.2015.1059835

QGIS Development Team. (2023). QGIS Geographic Information System. *Open Source Geospatial Foundation Project*.

Rabenhorst, N. C., Foss, J. E., & Fanning, D. S. (1982). Genesis of Maryland soils formed from serpentinite. *Soil Science Society of America Journal*, *46*(3), 607–616. https://doi.org/10.2136/sssaj1982.03615995004600030032x

Ralston, S. J., Hausrath, E. M., Tschauner, O., Rampe, E., Peretyazhko, T. S., Christoffersen, R., et al. (2021). Dissolution Rates of Allophane with Variable Fe Contents: Implications for Aqueous Alteration and the Preservation of X-Ray Amorphous Materials on Mars. *Clays and Clay Minerals*, *69*(2), 263–288. https://doi.org/10.1007/s42860-021-00124-x

Rampe, E. B., Blake, D. F., Bristow, T. F., Ming, D. W., Vaniman, D. T., Morris, R. V., et al. (2020). Mineralogy and geochemistry of sedimentary rocks and eolian sediments in Gale crater, Mars: A review after six Earth years of exploration with Curiosity. *Geochemistry*, *80*(2). https://doi.org/10.1016/j.chemer.2020.125605

Rampe, E. B., Horgan, B. H. N., Smith, R. J., Scudder, N. A., Bamber, E. R., Rutledge, A. M., & Christoffersen, R. (2022). A mineralogical study of glacial flour from Three Sisters, Oregon: An analog for a cold and icy early Mars. *Earth and Planetary Science Letters*, *584*. https://doi.org/10.1016/j.epsl.2022.117471

Rasmussen, C., Dahlgren, R. A., & Southard, R. J. (2010). Basalt weathering and pedogenesis across an environmental gradient in the southern Cascade Range, California, USA. *Geoderma*, *154*(3–4), 473–485. https://doi.org/10.1016/j.geoderma.2009.05.019

Ruff, S. W., & Hamilton, V. E. (2017). Wishstone to Watchtower: Amorphous alteration of plagioclase-rich rocks in Gusev crater, Mars. *American Mineralogist*, *102*(2). https://doi.org/10.2138/am-2017-5618

Rutledge, A. M., Horgan, B. H. N., Havig, J. R., Rampe, E. B., Scudder, N. A., & Hamilton, T. L. (2018). Silica Dissolution and Precipitation in Glaciated Volcanic Environments and Implications for Mars. *Geophysical Research Letters*, *45*(15). https://doi.org/10.1029/2018GL078105

Salvatore, M., Truitt, K., Roszell, K., Lanza, N., Rampe, E., Mangold, N., et al. (2019). Investigating the role of anhydrous oxidative weathering on sedimentary rocks in the Transantarctic Mountains and implications for the modern weathering of sedimentary lithologies on Mars. *Icarus*, *319*. https://doi.org/10.1016/j.icarus.2018.10.007

Simas, F. N. B., Schaefer, C. E. G. R., Melo, V. F., Guerra, M. B. B., Saunders, M., & Gilkes, R. J. (2006). Clay-sized minerals in permafrost-affected soils (Cryosols) from King George Island, Antarctica. *Clays and Clay Minerals*, *54*(6), 721–736. https://doi.org/10.1346/CCMN.2006.0540607

Skinner, C. N., Taylor, A. H., & Agee, J. K. (2006). Klamath Mountains bioregion. *Fire in California's Ecosystems*, (Irwin 1966), 170–194.

Smith, R. J., & Horgan, B. H. N. (2021). Nanoscale Variations in Natural Amorphous and Nanocrystalline Weathering Products in Mafic to Intermediate Volcanic Terrains on Earth: Implications for Amorphous Detections on Mars. *Journal of Geophysical Research: Planets*, *126*(5), 1–30. https://doi.org/10.1029/2020JE006769

Smith, R. J., McLennan, S. M., Achilles, C. N., Dehouck, E., Horgan, B. H. N., Mangold, N., et al. (2021). X-Ray Amorphous Components in Sedimentary Rocks of Gale Crater, Mars: Evidence for Ancient Formation and Long-Lived Aqueous Activity. *Journal of Geophysical Research: Planets*, *126*(3). https://doi.org/10.1029/2020JE006782

Szponar, N., Brazelton, W. J., Schrenk, M. O., Bower, D. M., Steele, A., & Morrill, P. L. (2013). Geochemistry of a continental site of serpentinization, the Tablelands Ophiolite, Gros Morne National Park: A Mars analogue. *Icarus*, *224*(2), 286–296. https://doi.org/10.1016/j.icarus.2012.07.004

Tarnas, J. D., Mustard, J. F., Lin, H., Goudge, T. A., Amador, E. S., Bramble, M. S., et al. (2019). Orbital Identification of Hydrated Silica in Jezero Crater, Mars. *Geophysical Research Letters*, *46*(22), 12771–12782. https://doi.org/10.1029/2019GL085584

Thorpe, M. T., Hurowitz, J. A., & Siebach, K. L. (2021). Source-to-Sink Terrestrial Analogs for the Paleoenvironment of Gale Crater, Mars. *Journal of Geophysical Research: Planets*, *126*(2). https://doi.org/10.1029/2020JE006530

Thorpe, M. T., Bristow, T. F., Rampe, E. B., Tosca, N. J., Grotzinger, J. P., Bennett, K. A., et al. (2022). Mars Science Laboratory CheMin Data From the Glen Torridon Region and the Significance of Lake-Groundwater Interactions in Interpreting Mineralogy and Sedimentary History. *Journal of Geophysical Research: Planets*, *127*(11). https://doi.org/10.1029/2021JE007099

Tosca, N. J., & Knoll, A. H. (2009). Juvenile chemical sediments and the long term persistence of water at the surface of Mars. *Earth and Planetary Science Letters*, *286*(3–4), 379–386. https://doi.org/10.1016/j.epsl.2009.07.004

Tutolo, B. M., Evans, B. W., & Kuehner, S. M. (2019). Serpentine–Hisingerite solid solution in altered ferroan peridotite and Olivine Gabbro. *Minerals*, *9*(1), 1–14. https://doi.org/10.3390/min9010047

Wada, K. (1989). Allophane and Imogolite. In *Minerals in Soil Environments* (pp. 1051–1087).

Weitz, C. M., Bishop, J. L., Baker, L. L., & Berman, D. C. (2014). Fresh exposures of hydrous Fe-bearing amorphous silicates on Mars. *Geophysical Research Letters*, *41*(24), 8744–8751. https://doi.org/10.1002/2014GL062065

Yesavage, T., Thompson, A., Hausrath, E. M., & Brantley, S. L. (2015). Basalt weathering in an Arctic Mars-analog site. *Icarus*, *254*, 219–232. https://doi.org/10.1016/j.icarus.2015.03.011

Ziegler, K., Hsieh, J. C. C., Chadwick, O. A., Kelly, E. F., Hendricks, D. M., & Savine, S. M. (2003). Halloysite as a kinetically controlled end product of arid-zone basalt weathering. *Chemical Geology*, *202*(3–4), 461–478. https://doi.org/10.1016/j.chemgeo.2002.06.001